Electronic Supplementary Material (ESI) for Lab on a Chip.
This journal is © The Royal Society of Chemistry 2021

Supplementary Information

High-throughput microfluidic compressibility cytometry using multi-tilted-angle surface acoustic wave

Yanqi Wu[1], Alastair G. Stewart[2,3] and Peter V.S. Lee[1]

[1]Department of Biomedical Engineering, University of Melbourne, Melbourne, VIC 3010, Australia
[2]Department of Biochemistry and Pharmacology, University of Melbourne, Melbourne, VIC 3010, Australia
[3]ARC Centre for Personalised Therapeutics Technologies, Melbourne, VIC 3010, Australia

Analytical simulation of multi-tilted-angle compressibility cytometry

As described in the Working Principle section, the trajectory of a particle subjected to the flow and the acoustics tilted by an angle can be determined by the equation (4). Hence, the simulation of the compressibility cytometry with a set of decreasing angles can be done by iteratively solving the equation (4). The process involves solving one iteration, transition from one iteration to the next and consideration of actual focusing band.

At the first iteration, the equation (4) was solved using the solver ode15s in MATLAB with the initial condition $y = y_0$ (where y_0 denotes the y coordinate of the initial position) and the x span from $x = 0$ to $x = L_0$ (where L_0 denotes the segment length). Due to the rectangular cross section of microchannel, the flow velocity profile per unit flow rate $u(y)$ was analytically defined as below.[1]

$$u(y) = \frac{48}{\left[1 - 0.630\frac{h}{w}\right]\pi^3 h w^{n,odd} n^3} \sum_{n}^{\infty} \frac{1}{n^3}\left[1 - \frac{\cosh\left(n\pi\frac{y}{h}\right)}{\cosh\left(n\pi\frac{w}{2h}\right)}\right]\sin\left(\frac{n\pi}{2}\right) \tag{S1}$$

where h and w denote the height and width of microchannel. In the equation (S1), the vertical position of particle in the microchannel was assumed to be at the half channel height, as the effect of vertical focusing was reported in the previous studies.[2,3] Furthermore, any possible discrepancies from the assumed vertical position will result in a constant scale-down for $u(y)$, which will be considered or corrected in the calibration process for the constant C in the equation (4).

In the following iterations, there were two changes made from the last iteration. Firstly, the coordinate system was translated and rotated to the one with respect to the current segment (with the origin at the centre of segment entrance and with the x-axis parallel to the channel). Secondly, the initial condition was set as the last position from the last iteration, that is, the

initial condition of the ith iteration was $y_0^i = y_{end}^{i-1}$. The rest was the same as the previous iterations.

After solving all the iterations, the trajectory of the particle starting from $y = y_0$ can be determined and the hitting position (where the y coordinate reached $w/2$) can be extracted for given constant C, input voltage V_I, flow rate Q and particle property ψ. Hence, the simulated hitting position was represented as $h = h\left(C\frac{V_I^2}{Q}, \psi, y_0\right)$ as shown in Fig. S1(a).

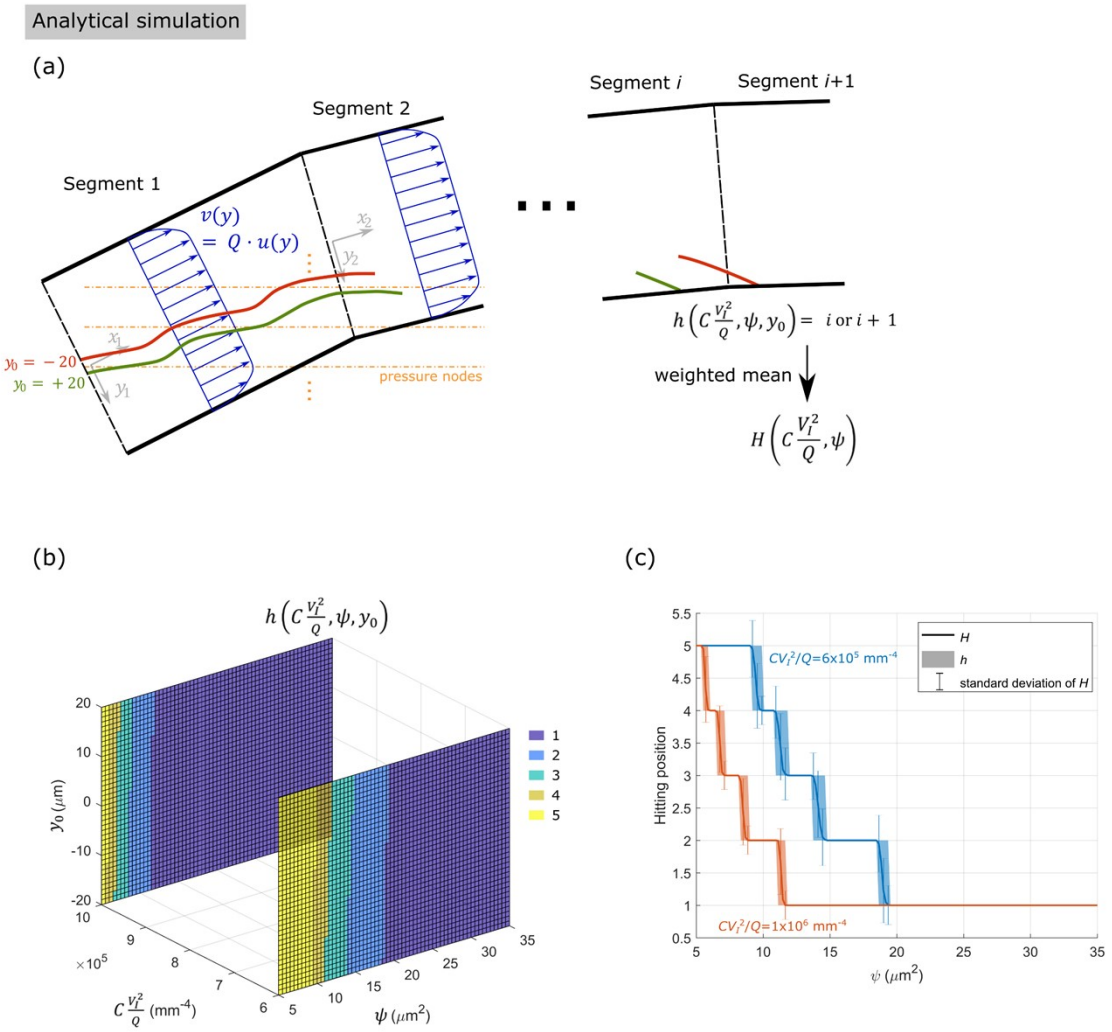

Fig. S1 (a) Schematic of the workflow of the analytical simulation. (b) Simulated hitting position $h\left(C\frac{V_I^2}{Q},\psi,y_0\right)$. (c) Comparison between the hitting position $h\left(C\frac{V_I^2}{Q},\psi,y_0\right)$ and the weighted mean hitting position $H\left(C\frac{V_I^2}{Q},\psi\right)$ and standard deviation of $H\left(C\frac{V_I^2}{Q},\psi\right)$.

In reality, the initial condition y_0 does not necessarily take the value of zero due to the hydrodynamic focusing forming a band instead of a line. The width of focusing band in our device was measured as approximately 40 μm. Hence, y_0 needs to take a value from -20 to 20 μm. We assumed it follows a normal distribution $Y_0 \sim N(0,(20/3)^2)$. Then, the final hitting position H was the weighted mean of the hitting position h weighted by the probability density function $f_{Y_0}(y_0)$ (Fig. S1(a)).

$$H\left(C\frac{V_I^2}{Q},\psi\right) = \int h\left(C\frac{V_I^2}{Q},\psi,y_0\right) \cdot f_{Y_0}(y_0) \cdot d(y_0) \tag{S2}$$

The hitting position $h\left(C\frac{V_I^2}{Q},\psi,y_0\right)$ was simulated across ranges of $C\frac{V_I^2}{Q}$, ψ and y_0 values and shown in Fig. S1(b). It showed that an increase in ψ at a given $C\frac{V_I^2}{Q}$ leads to a stepwise decrease in the hitting position h. The hitting position h at each given $C\frac{V_I^2}{Q}$ and ψ is mostly constant across the range between $y_0 = \pm 20$ μm, or in transition covers only two neighbouring positions. The same trend was also observed in the comparison of the hitting position h and the weighted mean hitting position H in Fig. S1(c), indicating that the spreading particles in the focused band still hit the same position in most cases and split into two neighbouring positions only at the transition with a window of ~0.5 μm^2 in ψ. The transition windows are small compared with the range of ψ and the standard deviation of H within the window is maximum 0.5 accounting for the two neighbouring positions. Hence, the transition could be negligible in the current setup, and the spreading of focused band has a minimal effect on the hitting position.

Comparison between analytical simulation and CFD simulation: a case study

The analytical simulation method as described above assumed a sharp turning of flow velocity profile at the boundary between two neighbouring segments, whereas the actual flow velocity may gradually turn the direction. Alternatively, a CFD model was created by COMSOL 4.3a (COMSOL Multiphysics) to provide a more accurate flow profile throughout the microchannel.

In the CFD simulation the flow field was calculated by the CFD model (Fig. S2(a)), followed by the equation solving for the equation (4), whereas in the analytical simulation the flow field was determined by the equation (S1) within the equation solving process for the equation (4). A case study of comparison between the two simulations was conducted for a microchannel with tilted angles from 27 to 15° with a decrement of 4° under $V = 20$ V_{pp} and $Q = 4$ μL/min . Then the hitting position H was plotted with regard to the particle property ψ (Fig. S2(b)).

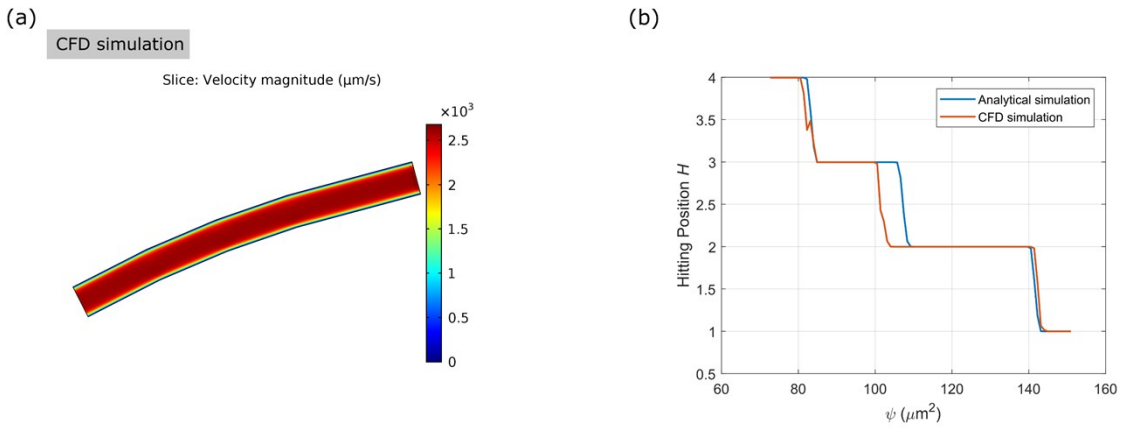

Fig. S2 (a) Simulated flow field by the CFD model. (b)Comparison of the simulated hitting position H between the analytical simulation and CFD simulation.

The results showed that the two simulations matched well and the maximum error in ψ is ~5%, suggesting that the analytical simulation was accurate enough despite the approximation at the boundary between two segments. On the other hand, the CFD simulation appeared to be computationally expensive as compared to the analytical simulation. In the CFD simulation, the flow field calculation took 1 minute for a given geometry and flow rate, and the equation solving took ~49 seconds for a given $C\frac{V_I^2}{Q}$ and ψ containing 20 trajectories within the y_0 range. In the analytical simulation, the flow field was determined within the equation solving process, and the equation solving took ~0.7 seconds for a given $C\frac{V_I^2}{Q}$ and ψ containing 20 trajectories within the y_0 range. Although the consumed time may be subject to algorithm optimisation and computer performance, the CFD simulation is expected to spend about 70 folds the time as the analytical simulation used to generate a map of $H\left(C\frac{V_I^2}{Q},\psi\right)$ as shown in Fig. 2(b), making it almost impossible to adopt the CFD simulation in our setup.

Due to the complexity in adjusting geometry and relatively high computational cost in the CFD simulation, the analytical simulation method was used in this study.

Prediction and device calibration by hitting position map

With the hitting position map, the behaviour of particles with known properties can be predicted under any given condition. The property values used for the predictions for 10-µm PS, 10-µm PMMA and 15-µm PS microbeads were summarised in the table as below.

	R (µm)	β_P (× 10^{-10} Pa^{-1})	ρ_P (kg/m^3)	β_m (× 10^{-10} Pa^{-1})	ρ_m (kg/m^3)	ψ (μm^2)
10-µm PS	5	2.16 [4]	1050 [4,5]	4.6	997	14.5
10-µm PMMA	5	1.73 [6]	1200 [6]	4.6	997	20.0
10-µm PS	7.5	2.16 [4]	1050 [4,5]	4.6	997	32.6

Table. S1 Property values used for the predictions for 10-µm PS, 10-µm PMMA and 15-µm PS microbeads

In addition to the property values given in the table S1, the property variation of a population also needs to be considered. In our previous study,[7] the ψ of 10-µm PS microbeads showed a standard deviation of 1.04 μm^2 or a variation of 7%, as a result of the variations in the measured radius and compressibility. Hence, we assumed a variation of 7% for the ψ of each microbead population, which followed a normal distribution $\Psi_{bead} \sim N\left(\psi_{bead}, (\psi_{bead} \times 7\%)^2\right)$ and a probability density function $f_{\Psi_{bead}}(\psi)$. The predicted hitting position for a microbead population can be calculated as a weighed mean across the range of ψ.

$$H_{bead}\left(C\frac{V_I^2}{Q}\right) = \int H\left(C\frac{V_I^2}{Q}, \psi\right) \cdot f_{\Psi_{bead}}(\psi) \cdot d\psi \tag{S3}$$

In the calibration process, hundreds of 10-µm PS microbeads were tested under different combinations of input voltage V_I and flow rate Q. The hitting position was experimentally obtained as $\hat{H}_{bead}$ and then compared with the predicted hitting position H_{bead}. Then the constant C can be determined by $C = \min_C \left[\sum_{V_I, Q}\left(H_{bead}\left(C\frac{V_I^2}{Q}\right) - \hat{H}_{bead}\left(\frac{V_I^2}{Q}\right)\right)^2\right]$. For example, the constant C for the chip used in this study had a value of 6.439×10^4, with the confidence interval of [6.369×10^4 6.509×10^4] and the standard error of 252, when input voltage V_I was in V and flow rate Q was in m^3/s.

Error analysis

An error analysis was conducted to examine the impacts on the measured compressibility of several experimental parameters including the calibrated constant C, cell density and radius. It was done by perturbing the parameters around their initial values by up to 5%. The initial values were determined by the properties from the MDA MB231 cell experiment, which were 6.439 × 10^4 for the calibrated constant, 7.3 μm for the cell radius and 1,050 kg/m^3 for the cell density. They will give a compressibility measurement of 3.64 ×10^4 Pa^{-1} given the input voltage of 28 V_{pp}, flow rate of 5.5 μL/min and hitting position of 3. The change in the measured compressibility in response to the experimental parameter perturbation was then calculated and the results are presented both in percentage (Fig. S3).

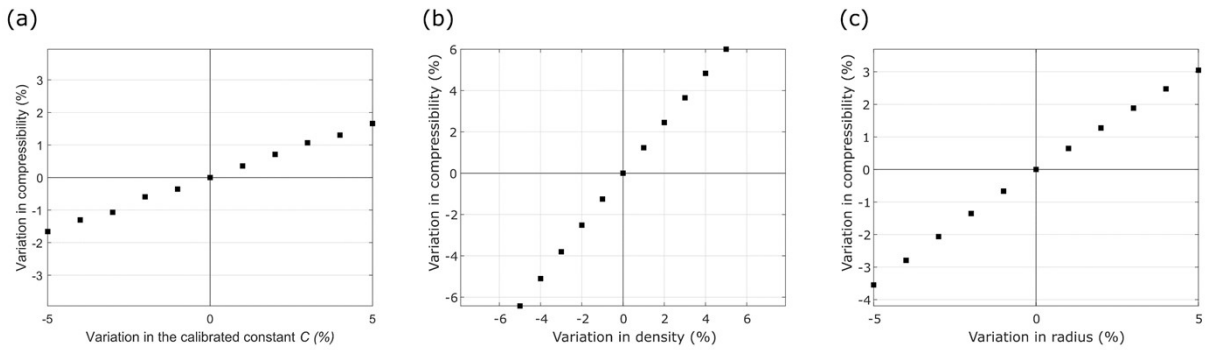

Fig. S3 Error analysis for the impacts of (a) calibrated constant C, (b) cell density and (c) cell radius on the final measured compressibility.

The standard error of the calibrated constant C, equivalent to the variation of 0.3%, would lead to a variation of 0.1% in the measured compressibility (Fig. S3(a)). The single-cell density was assumed to be constant throughout this study, and it may lead to an error due to the density variation in cell populations reported in the literature. Human lung cancer cells (H1650) and human erythrocytes were reported to have a density distribution ranging 1,040 – 1,060 kg/m^3 and 1,070 – 1,095 kg/m^3 in two separate studies, respectively.[8,9] Mouse erythrocytes, mouse lymphocytes and Chinese hamster epithelial cells (CHO) were reported to have a density distribution ranging 1,065 – 1,090 kg/m^3, 1,050 – 1,090 kg/m^3 and 1,050 – 1,070 kg/m^3 of in three separate studies, respectively.[10–12] All these studies suggest the absolute density variation of about ±15 kg/m^3 in mammalian cell lines. It accounts for a variation of 1.4% in the cell density in this study and this variation in cell density would lead to a variation of 2% in the measured compressibility (Fig. S3(b)). As reported in our previous study which adopted the same microscopy and image analysis for radius measurement, the measured radius had an error

of 0.6%.[7] The error in radius would lead to a variation of 0.4% in the measured compressibility (Fig. S3(c)).

In order to improve the system design and further reduce the impact of density variation, the mathematical definition of the acoustic contrast factor, $\varphi = \frac{5\rho_P - 2\rho_m}{2\rho_P + \rho_m} - \frac{\beta_P}{\beta_m}$ (where ρ denotes density, β denotes compressibility and the subscripts P and m denote particle and medium), needs to be investigated. The derivative can be determined as $d\varphi = \frac{9\rho_P\rho_m}{(2\rho_P + \rho_m)^2} \frac{d\rho_P}{\rho_P} - \frac{\beta_P d\beta_P}{\beta_m \beta_P}$. Hence, the dimensionless parameters $\frac{9\rho_P\rho_m}{(2\rho_P + \rho_m)^2}$ and $\frac{\beta_P}{\beta_m}$ can be seen as the contributions of density variation and compressibility variation, respectively. The density contribution parameter $\frac{9\rho_P\rho_m}{(2\rho_P + \rho_m)^2} = \frac{9}{4\frac{\rho_P}{\rho_m} + \frac{\rho_m}{\rho_P} + 4}$ reaches the maximum when $\rho_m = 2\rho_P$ and decreases when ρ_m is further away from $2\rho_P$. The compressibility contribution parameter $\frac{\beta_P}{\beta_m}$ increases when β_m decreases. In practice, the density and compressibility of medium can be tuned by the addition of high-molecule weight solution such as OptiPrep iodixanol solution[13] or Ficoll solution,[14] and therefore the contribution of density variation can be reduced with regard to that of compressibility. The solution concentration needs to be optimised for the largest contrast between the two parameters and its impact on cell behaviours such as cell viability also requires additional investigation.

Full measurement data

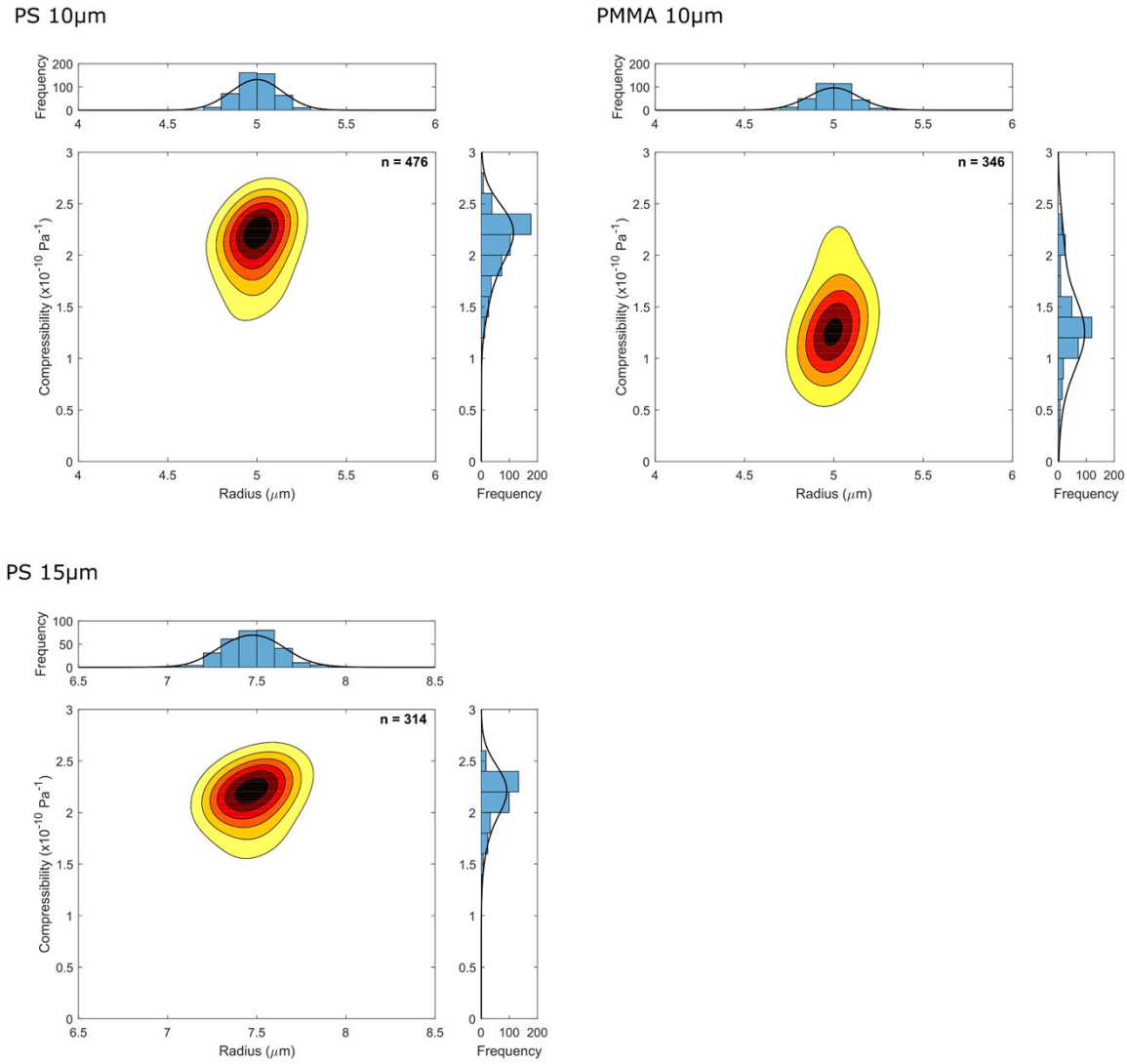

Fig. S4 Full data for the measurement of microbeads

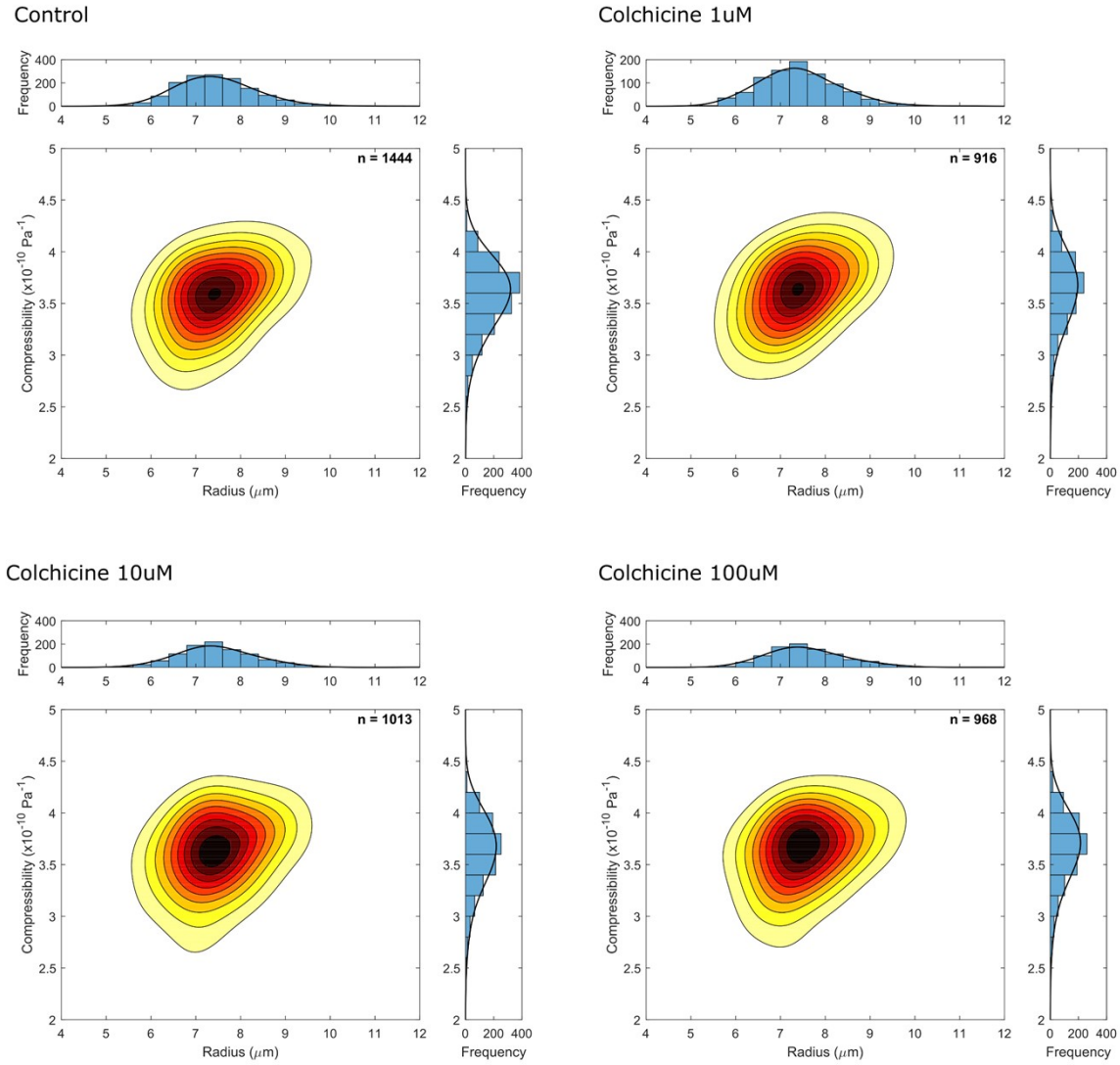

Fig. S5 Full data for the measurement of microtubule-disrupted cells

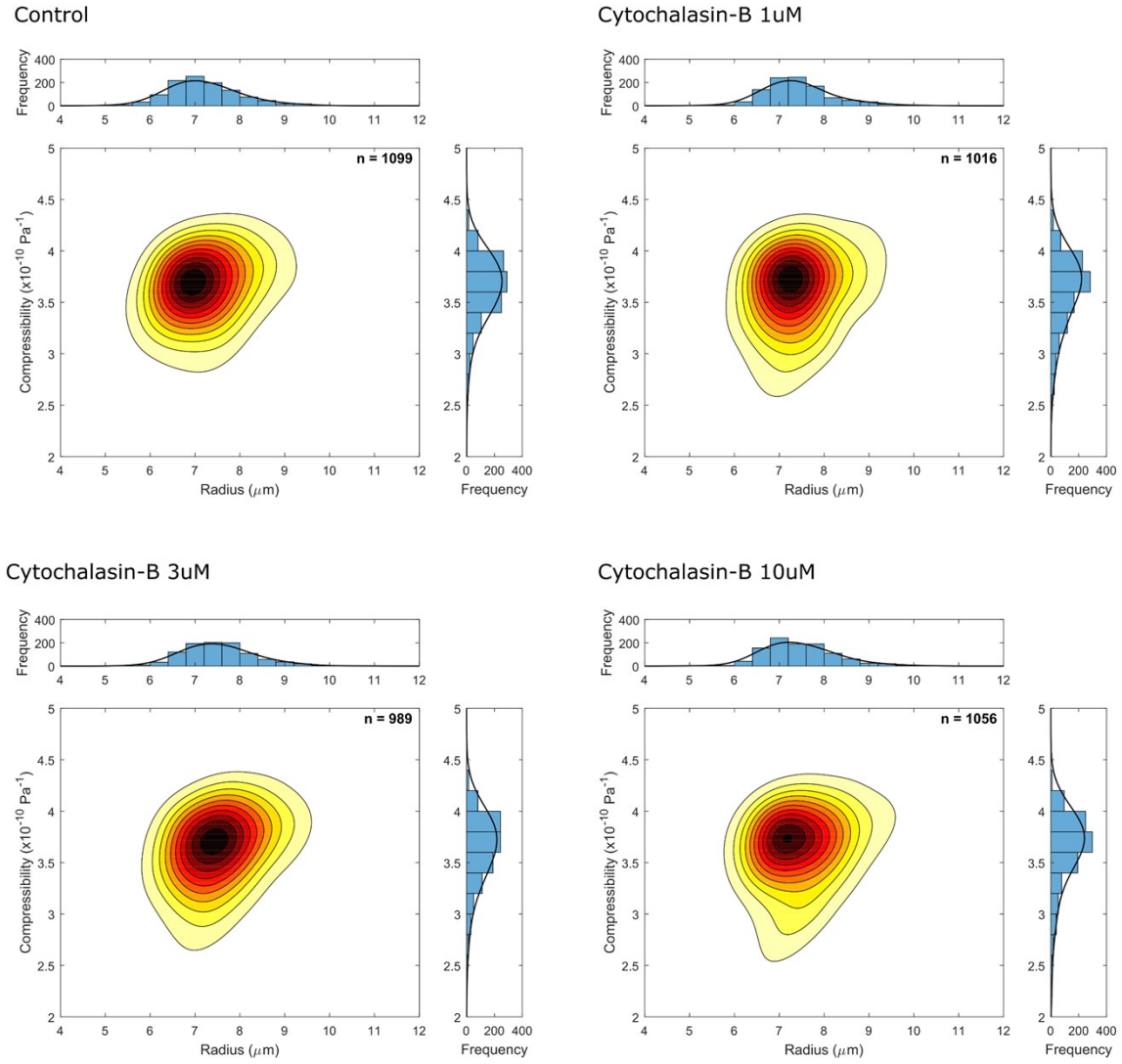

Fig. S6 Full data for the measurement of actin-disrupted cells

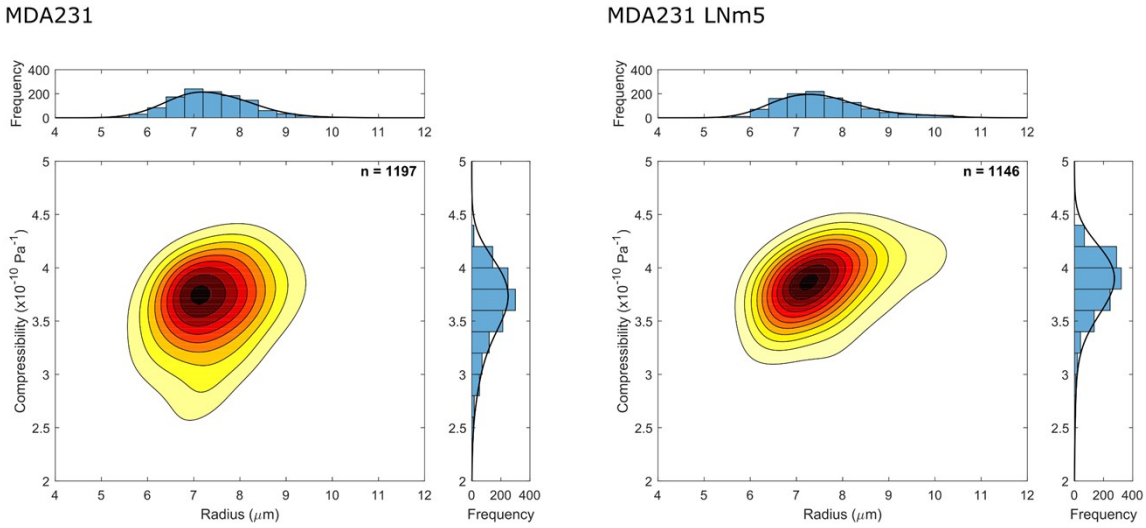

Fig. S7 Full data for the measurement of cancer cells with different metastatic potential

References

1 H. Bruus, *Lab on a Chip*, 2011, **11**, 3742.
2 D. J. Collins, T. Alan and A. Neild, *Lab Chip*, 2014, **14**, 1595–1603.
3 Y. Chen, A. A. Nawaz, Y. Zhao, P.-H. Huang, J. P. McCoy, S. J. Levine, L. Wang and T. J. Huang, *Lab Chip*, 2014, **14**, 916–923.
4 X. Ding, Z. Peng, S.-C. S. Lin, M. Geri, S. Li, P. Li, Y. Chen, M. Dao, S. Suresh and T. J. Huang, *Proceedings of the National Academy of Sciences*, 2014, **111**, 12992–12997.
5 D. Hartono, Y. Liu, P. L. Tan, X. Y. S. Then, L.-Y. L. Yung and K.-M. Lim, *Lab on a Chip*, 2011, **11**, 4072.
6 K. W. Cushing, F. Garofalo, C. Magnusson, L. Ekblad, H. Bruus and T. Laurell, *Analytical Chemistry*, 2017, **89**, 8917–8923.
7 Y. Wu, A. G. Stewart and P. V. S. Lee, *Biomicrofluidics*, 2019, **13**, 024107.
8 A. K. Bryan, V. C. Hecht, W. Shen, K. Payer, W. H. Grover and S. R. Manalis, *Lab on a Chip*, 2014, **14**, 569–576.
9 R. C. Leif and J. Vinograd, *Proceedings of the National Academy of Sciences*, 1964, **51**, 520–528.
10 J. T. Thornthwaite and R. C. Leif, *J Immunol*, 1975, **114**, 1023–1033.
11 K. Shortman, *J. Cell. Physiol.*, 1971, **77**, 319–329.
12 E. C. Anderson, D. F. Petersen and R. A. Tobey, *Biophysical Journal*, 1970, **10**, 630–645.
13 P. Augustsson, J. T. Karlsen, H. W. Su, H. Bruus and J. Voldman, *Nature Communications*, 2016, **7**, 1–9.
14 Y. Xie, Z. Mao, H. Bachman, P. Li, P. Zhang, L. Ren, M. Wu and T. J. Huang, *Journal of Biomechanical Engineering*, 2020, **142**, 031005.